Article

Prediction of Breakdown Pressure Using a Multi-Layer Neural Network Based on Supercritical CO$_2$ Fracturing Data

Xiufeng Zhang [1], Min Zhang [2,*], Shuyuan Liu [3] and Heyang Liu [3]

1   Department of Geotechnical Engineering, Tongji University, Shanghai 200092, China; xiufeng_zhang@tongji.edu.cn
2   Geotechnical Institute, TU Bergakademie Freiberg, 09599 Freiberg, Germany
3   School of Resource and Civil Engineering, Northeastern University, Shenyang 110819, China; shuyuanliu@stumail.neu.edu.cn (S.L.); 2210446@stu.neu.edu.cn (H.L.)
*   Correspondence: minzhangtubaf@gmail.com

Abstract: Hydraulic fracturing is a widely employed technique for stimulating unconventional shale gas reservoirs. Supercritical CO$_2$ (SC-CO$_2$) has emerged as a promising fracturing fluid due to its unique physicochemical properties. Existing theoretical models for calculating breakdown pressure often fail to accurately predict the outcomes of SC-CO$_2$ fracturing due to the complex, nonlinear interactions among multiple influencing factors. In this study, we conducted fracturing experiments considering parameters such as fluid type, flow rate, temperature, and confining pressure. A fully connected neural network was then employed to predict breakdown pressure, integrating both our experimental data and published datasets. This approach facilitated the identification of key influencing factors and allowed us to quantify their relative importance. The results demonstrate that SC-CO$_2$ significantly reduces breakdown pressure compared to traditional water-based fluids. Additionally, breakdown pressure increases with higher confining pressures and elevated flow rates, while it decreases with increasing temperatures. The multi-layer neural network achieved high predictive accuracy, with R, RMSE, and MAE values of 0.9482 (0.9123), 3.424 (4.421), and 2.283 (3.188) for training (testing) sets, respectively. Sensitivity analysis identified fracturing fluid type and tensile strength as the most influential factors, contributing 28.31% and 21.39%, respectively, followed by flow rate at 12.34%. Our findings provide valuable insights into the optimization of fracturing parameters, offering a promising approach to better predict breakdown pressure in SC-CO$_2$ fracturing operations.

Keywords: supercritical CO$_2$; hydraulic fracturing; breakdown pressure prediction; multi-layer neural network; laboratory data

1. Introduction

Hydraulic fracturing has been extensively employed as a reservoir stimulation technique in the development of unconventional shale gas resources. In recent years, CO$_2$-based fracturing fluids have emerged as a promising alternative to traditional water-based fluids, offering several technical advantages, such as minimal damage to the reservoir, improved fluid recovery, and the dual benefits of enhancing methane desorption and enabling CO$_2$ sequestration [1]. When injected CO$_2$ exceeds its critical temperature of 31.1 °C and critical pressure of 7.38 MPa, it transitions to a supercritical state [2]. Supercritical CO$_2$ (SC-CO$_2$) exhibits unique physicochemical properties, such as low viscosity, near-zero surface tension, high diffusion coefficients, and a density approaching that of water. These properties contribute to its superior heat and mass transfer capabilities, making SC-CO$_2$ fracturing a promising technology for stimulating unconventional oil and gas reservoirs [3,4].

Breakdown pressure remains one of the key parameters in assessing fracturing effectiveness. Mathematical models for calculating breakdown pressure are widely used in the analysis of fracturing mechanisms. Traditional models are predominantly based on elasticity theory and fracture mechanics, focusing on tensile or shear strength criteria [5].

Among these models, the calculation of breakdown pressure based on tensile strength is the most prevalent. Hubbert and Willis [6] first proposed a formula to calculate breakdown pressure, which was later refined by Haimson and Fairhurst [7] to incorporate the effects of rock permeability. Additionally, the point-stress model proposed by Ito [8] (i.e., Ito model) suggests that fracturing initiates at the borehole wall when a point within the rock, at a certain distance from the wall, reaches the tensile strength of the rock. Experiments conducted by Li et al. [9] on cylindrical shale specimens using liquid CO_2 (L-CO_2), water, and nitrogen led to a modified fitting formula for breakdown pressure; however, it does not account for the influence of fluid properties associated at different CO_2 phases, particularly under varying confining and axial pressures. In the context of SC-CO_2 fracturing, Chen et al. [10] developed a breakdown pressure prediction model incorporating the unique properties of SC-CO_2. This model, based on Ito's [8] equation for fluid pressure distribution, was compared with hydraulic fracturing results. However, significant discrepancies between laboratory experiments and theoretical predictions were observed. Currently, no universal theoretical model exists that can fully explain the abnormal pressure phenomena observed in SC-CO_2 fracturing experiments.

Due to the high costs and resource demands of large-scale field operations, most current research on hydraulic fracturing relies on laboratory-scale physical simulations. However, these experiments present their challenges, such as complex testing processes, extended durations, and significant variability in rock properties. To address these limitations, researchers have increasingly turned to artificial intelligence (AI) methods to investigate fracturing stimulation issues. Specifically, these methods have been applied in predicting reservoir geological parameters (Zhang and Chen [11]), calibrating the constitutive model [12], optimizing fracturing design parameters [13], evaluating fracturing effectiveness [14], predicting shale gas sweet spots [15], and developing fracturing tools and materials [16]. In the context of the fracturing effectiveness, Gao [17] employed neural networks and AI algorithms such as stepwise regression to predict fracturing effectiveness based on field data. Similarly, Yan [18] developed a hybrid intelligent model combining a Discrete Grey Wolf Optimizer (DGWO) combined with a Support Vector Machine (SVM) to predict outcomes in SC-CO_2 fracturing. The model's performance was evaluated using correlation coefficients and root mean square error, while sensitivity analysis was conducted using the Mean Impact Value method. Subsequently, Yan et al. [19] developed a hybrid AI model integrating a Backpropagation Neural Network, an Extreme Learning Machine, and SVM, using input factors such as vertical and horizontal principal stresses, injection volume, tensile strength, elastic modulus, and Poisson's ratio to predict breakdown pressure for SC-CO_2 fracturing.

Given the complexity of the factors influencing breakdown pressure in SC-CO_2 fracturing, traditional mathematical models often fail to provide accurate predictions. In contrast, deep learning offers a promising alternative by automatically learning hierarchical representations of data, enabling complex functions to be mapped from inputs to outputs without predefined assumptions [20]. By capturing the intricate relationships between multiple factors, deep learning models can identify key variables influencing SC-CO_2 breakdown pressure and provide reliable predictive outcomes.

In this study, we first conducted fracturing experiments to obtain breakdown pressure, considering influencing factors such as fracturing fluid type, flow rate, temperature, and confining pressure. We then compared experimental data with values calculated from breakdown pressure models based on elasticity theory. Key influencing factors were identified, and additional indoor fracturing data from the literature were incorporated with our experimental results to create a comprehensive dataset. A fully connected neural network was then applied to predict breakdown pressure and assess the relative importance of each factor. This integrated methodology significantly enhances our understanding of breakdown pressure in SC-CO_2 fracturing, and provides valuable insights for optimizing fracturing operations.

2. Fracturing Tests

2.1. Rock Specimens and Apparatus

The experimental specimens were Longmaxi shales collected from outcrops in Changning (labeled as CN-Shale) and Pengshui (labeled as PS-Shale), both located in the Sichuan Basin, China. Figure 1 shows the flow chart of the shale specimen preparation. The prepared specimens were used in hydraulic fracturing experiments to determine the breakdown pressure, and in basic tests to measure the rock's petrophysical and mechanical properties, including bulk density, tensile strength, compressive strength, P-wave velocity, and water content (Table 1). The processing requirements of the shales for these basic tests adhered to International Society of Rock Mechanics standards.
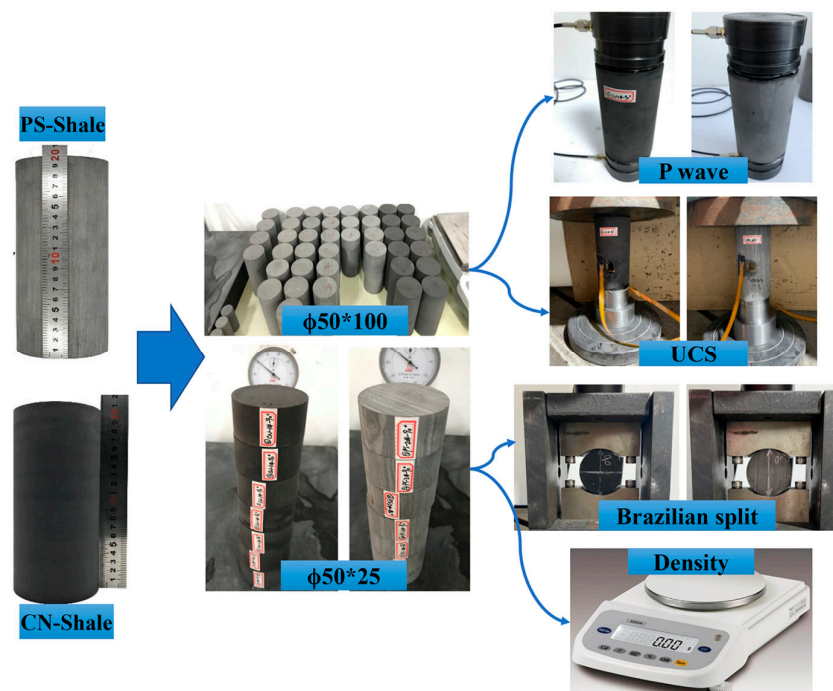

Figure 1. Flow chart of the shale specimen preparation for the experiments. UCS denotes uniaxial compressive strength. $\phi 50 * 100$ and $\phi 50 * 25$ denote cylindrical specimens with a diameter of 50 mm and heights of 100 mm and 25 mm, respectively. "ϕ" is the symbol that typically represents diameter, and "$*$" is a notation for the dimension.

Table 1. Average values of basic parameters of shale.

Parameters	CN-Shale	PS-Sahle	Units
Bulk density, ρ_s	2546	2648	kg/m^3
Elastic modulus, E	12.16	11.99	GPa
Poisson's ratio, ν	0.20	0.25	—
Tensile strength, σ_t	15.63	18.18	MPa
Compressive strength, σ_c	151.55	138.45	MPa
P-wave velocity, v_p	5.00	4.47	km/s
Water content, w	0.4	0.3	%
Sampling site	Changning	Pengshui	—
Bedding orientation	Perpendicular	Perpendicular	—

As shown in Figure 2, the shale specimens used for fracturing had a diameter of 100 mm and height of 200 mm, with a central borehole of 10 mm in diameter and 110 mm in height, leaving an open hole section with a depth of 40 mm. The shale bedding planes were oriented perpendicularly, with the borehole drilled parallel to the bedding planes.

The packer fixing method for sealing and forming the open hole was described in detail by Zhu et al. [21] and Zhang et al. [22].
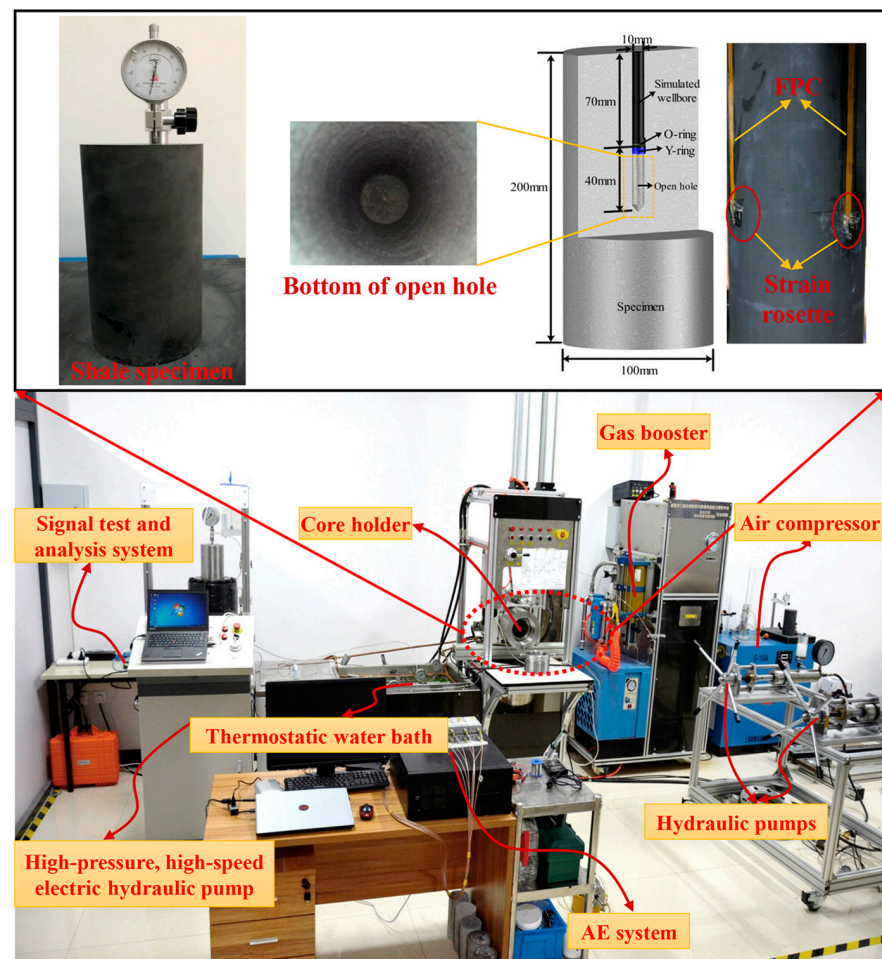

Figure 2. Experimental apparatus used for hydraulic fracturing tests. AE refers to acoustic emission, while FPC stands for flexible printed circuit.

Figure 2 shows the experimental apparatus used for hydraulic fracturing tests, which consisted of six main modules, as follows: (1) gas supply; (2) water supply; (3) axial and confining pressure loading; (4) vacuuming; (5) temperature control; and (6) seepage testing. These modules operate collaboratively to achieve specific functions. Further design and functionality details are available in the work of Zhu et al. [21]. This apparatus enables fracturing experiments using various injection fluids on shale under different in situ stress conditions, reservoir temperatures, and flow rates, with real-time data acquisition of injection pressure, axial/confining pressure, temperature, strain, and acoustic emission (AE) signals during the fracturing process, as well as seepage testing when fractures propagate to the end face of the shale specimen. In this study, we merely concentrated on the breakdown pressure for providing experimental data.

2.2. Fracturing Schemes and Procedure

When analyzing fracturing performance, various factors need to be considered, including reservoir characteristics (e.g., geothermal gradient, in situ stress, weak planes, strength, porosity, and permeability) and operational parameters (e.g., fracturing fluid type, perforation, completion, pump rate, and stage division) [23]. This study focused on the primary factors of fracturing fluid type, reservoir temperature, flow rate, and confining pressure.

Figure 3 illustrates the experimental schemes of fracturing. Specimens No. 1# to 5# (CN-Shales) were used to investigate the effects of fracturing fluid and flow rate, while specimens No. 6# to 11# (PS-Shales) focused on the effects of temperature and in situ stress.
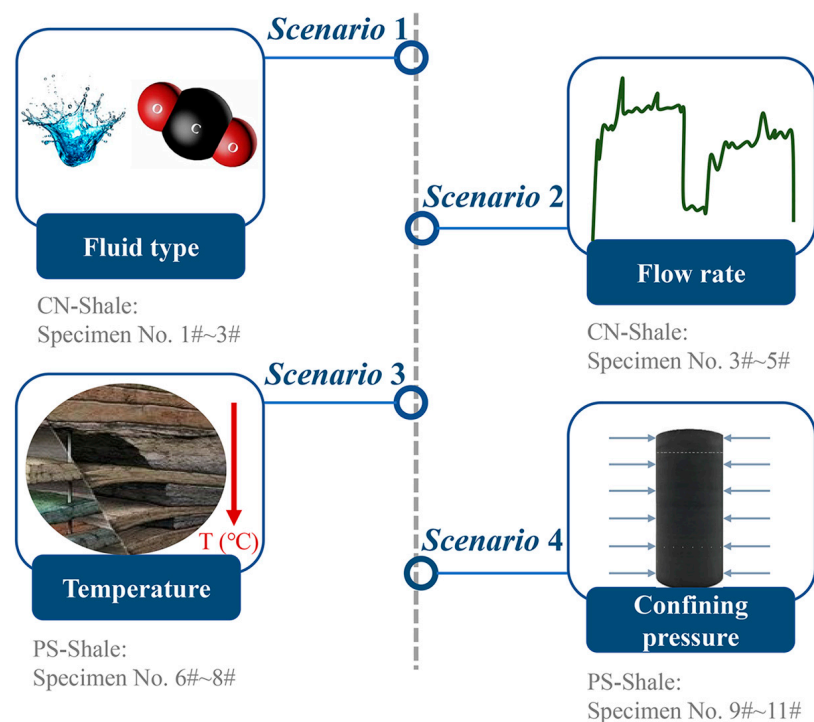
Figure 3. Fracturing experiment schemes.

As shown in Figure 2, each shale specimen was first placed into a triaxial core holder, which was then submerged in a thermostatic water bath to simulate reservoir temperature conditions. Two hydraulic pumps alternately applied axial and confining pressures to the specimen, replicating the in situ stress condition of the shale reservoir. Finally, the appropriate fracturing fluid was selected for injection based on the fracturing schemes. For hydraulic fracturing, deionized water was directly injected into the specimen using a high-pressure, high-speed electric hydraulic pump. SC-CO_2 fracturing, however, required a specialized SC-CO_2 preparation system, including a gas booster and an intermediate container. The gas booster pressurized CO_2 in the intermediate container beyond the critical pressure of 7.38 MPa, while the thermostatic water bath raised the CO_2 temperature above the critical threshold of 31.1 °C. This process produced SC-CO_2 at the required temperature and pressure, which was stored in the intermediate container and fracturing lines, establishing the starting condition for the fracturing experiment.

2.3. Experimental Results

The fracturing process is typically analyzed by monitoring the variation in injection pressure over time. The peak of the injection pressure curve, which corresponds to the first maximum fluid pressure, is identified as the breakdown pressure (denoted as P_b hereafter). Reaching this pressure signifies that the shale specimen is fractured [24,25]. To illustrate the injection pressure curve, the results from the flow rate have been provided as an example in Figure 4. In addition, since the primary focus of this study is breakdown pressure, the breakdown pressure values for each scenario are listed in Figure 5.
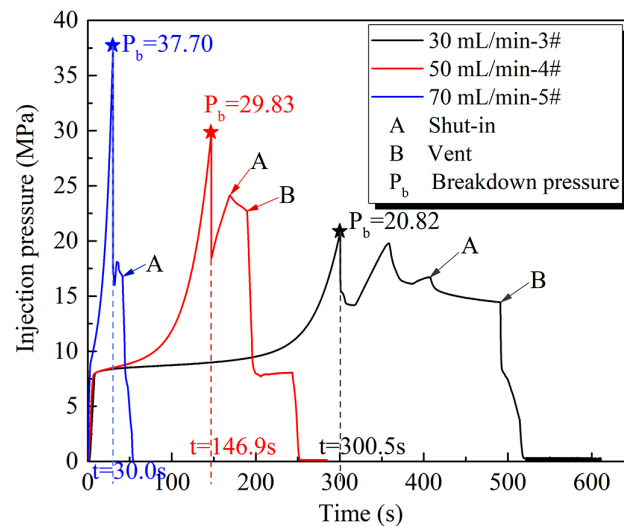
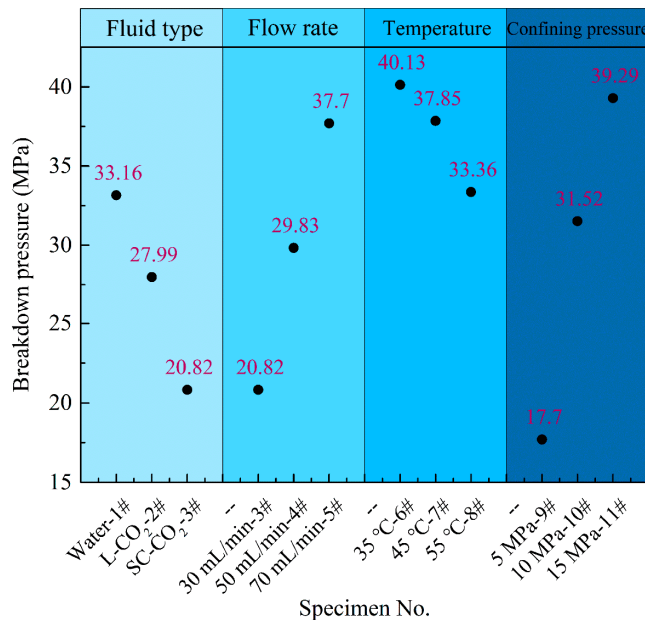**Figure 4.** Injection pressure versus time under various flow rates.

Figure 5. Breakdown pressure under different fracturing schemes.

A comparison of breakdown pressures under different flow rates has revealed that higher flow rates resulted in higher breakdown pressures. As shown in Figure 4, the breakdown pressures at flow rates of 70 mL/min, 50 mL/min, and 30 mL/min were 37.70 MPa, 29.83 MPa, and 20.82 MPa, respectively. Correspondingly, the times to reach breakdown pressure were 30.0 s, 146.9 s, and 300.5 s, indicating that higher flow rates can raise CO_2 injection pressure, causing shale failure more quickly.

As illustrated in Figure 5, the peak injection pressures for shale fracturing with water, L-CO_2, and SC-CO_2 were 33.16 MPa, 27.99 MPa, and 20.82 MPa, respectively. Compared to hydraulic fracturing with water, the breakdown pressure for SC-CO_2 decreased by 37.2%, and for L-CO_2, it decreased by 15.6%. This reduction may be attributed to the high diffusivity and superior penetrability of SC-CO_2, which enables it to infiltrate microfractures and natural crack tips, significantly enhancing its rock-breaking capability.

Figure 5 shows that when the temperature increased from 35 °C to 45 °C and 55 °C, the breakdown pressure of the shale specimens decreased from 40.13 MPa to 37.85 MPa and 33.36 MPa, corresponding to reductions of 5.68% and 16.87%, respectively. This trend aligns with the findings of Lu et al. [26]. Two potential explanations are available, as follows: First,

higher temperatures reduce the viscosity and increase the diffusivity of SC-CO$_2$, resulting in lower breakdown pressures. Second, the thermal stress generated within the shale decreases the effective stress on the mineral matrix, further contributing to the reduction in breakdown pressure.

Based on the theory of linear elastic tensile failure, the breakdown pressure models proposed by Hubbert and Willis [6] (commonly referred to as the H-W model) and Haimson and Fairhurst [7] (referred to as the H-F model) primarily account for the influences of horizontal stress and tensile strength. In this study, we varied the confining pressure to investigate the impact of in situ stress on breakdown pressure. As illustrated in Figure 4, higher confining pressures necessitated larger injection pressures to induce rock failure. Specifically, at a confining pressure of 5 MPa, the breakdown pressure was measured at 17.70 MPa. When the confining pressure was increased to 10 MPa and 15 MPa, the breakdown pressures rose by 43.85% and 54.95%, respectively.

3. Theoretical Models for Calculating Breakdown Pressure

3.1. Theoretical Model Based on Elasticity Mechanics

Theoretical models used to predict hydraulic fracturing breakdown pressure are generally based on various assumptions. Common models include those based on linear elasticity, poroelasticity, characteristic distance, shear failure, energy release, and stress intensity factors [27,28]. Several factors influence the breakdown pressure, such as the viscosity of the fracturing fluid [29], the stress state of the rock surrounding the borehole [6], the size and orientation of the borehole [30,31], the pressurization rate [32,33], the formation pore pressure [8], rock mechanical properties [7], and the reservoir temperature [19].

Assuming the reservoir behaves as a homogeneous, isotropic, linear elastic porous medium, and the rock surrounding the central borehole (wellbore) is subjected to plane strain conditions, the stresses in the system can be categorized as tensile (positive) and compressive (negative). As illustrated in Appendix A, the total circumferential stress around the borehole consists of three components. Upon the injection of high-pressure fluid, the total stress distribution around the borehole is altered. This stress alteration can be evaluated through the principle of superposition, where the original in situ stresses combine with the additional stresses induced by the fluid injection. This superimposed stress field ultimately governs the breakdown pressure and fracture propagation in the surrounding rock mass.

When the circumferential effective stress σ_θ at the wellbore wall reaches the tensile strength of the rock (σ_t), failure occurs, in accordance with the Hubbert–Willis criterion (i.e., H-W model) [6]. This criterion is predicated on the assumption that the rock is impermeable. Consequently, the circumferential stress component resulting from pore pressure can be disregarded, leading to breakdown pressure primarily governed by in situ stress and injection pressure. Furthermore, the criterion posits that fractures initiate perpendicular to the minimum horizontal stress (i.e., $\theta = 0$ or π in Equation (A1)). The H-W breakdown pressure P_b can be calculated with or without accounting for the initial pore pressure P_0, as illustrated in Equations (1) and (2).

$$P_b = -\sigma_H + 3\sigma_h + \sigma_t - P_0 \tag{1}$$

$$P_b = -\sigma_H + 3\sigma_h + \sigma_t \tag{2}$$

In dense reservoirs, characterized by nanometer-scale permeability and the near incompressibility of water, hydraulic fracturing occurs rapidly, making fluid penetration negligible at the moment of injection and fracturing. As a result, the breakdown pressure for water as a fracturing fluid can be directly calculated using Equations (1) and (2). Conversely, SC-CO$_2$, with its low viscosity, absence of surface tension, and strong diffusion capabilities, demonstrates significant filtration effects. Consequently, the influence of pore pressure on breakdown pressure becomes significant and cannot be overlooked. This filtration effect introduces an additional circumferential stress component (σ_θ^3). Assuming that SC-

CO_2 penetrates the rock completely, the breakdown pressure can be determined using the Haimson–Fairhurst formula (i.e., H-F model) [7]. The H-F breakdown pressure P_b, which can be calculated with or without accounting for the initial pore pressure P_0, is expressed in Equations (3) and (4).

$$P_b = \frac{-\sigma_H + 3\sigma_h + \sigma_t - \alpha \frac{1-2\nu}{1-\nu} P_0}{2 - \alpha \frac{1-2\nu}{1-\nu}} \tag{3}$$

$$P_b = \frac{-\sigma_H + 3\sigma_h + \sigma_t}{2 - \alpha \frac{1-2\nu}{1-\nu}} \tag{4}$$

The breakdown pressure models discussed above assume that rock failure occurs at a specific point on the wellbore wall, and do not consider the actual fluid pressure distribution within the rock. Numerical simulations by Jia et al. [34] demonstrated that, prior to fracturing, $SC-CO_2$ infiltrates a significantly larger area of shale compared to water, which fails to penetrate to the characteristic distance defined by Ito [8]. The point-stress model proposed by Ito [8] provides a framework for explaining breakdown pressure during $SC-CO_2$ fracturing, as expressed in Equations (5) and (6). This model enhances previous approaches by incorporating the fluid pressure distribution outside the wellbore, allowing for a more accurate calculation of the circumferential stress component σ_θ^3. Additionally, it considers the effects of wellbore diameter and pressurization rate on breakdown pressure. The model posits that the location where the maximum effective stress surpasses the tensile strength of the rock is not at the wellbore wall, but rather at a point within the rock. The distance from this point to the wellbore wall is defined as the characteristic distance d_c, given by $d_c = K_{IC}^2 / (2\pi\sigma_t^2)$. Here, K_{IC} represents the mode I fracture toughness, MPa·m$^{0.5}$. Thus, the total circumferential stress (S_θ) and pore pressure distribution can be expressed as follows:

$$S_\theta = \left(\sigma_\theta^1 + \sigma_\theta^2 + \sigma_\theta^3\right)_{r=r_w+d_c} \tag{5}$$

$$p(r,t) = C \int_0^t f(r,t)dt + P_0 \tag{6}$$

where C denotes the wellbore pressurization rate, and $f(r,t)$ is defined as [8]:

$$f(r,t) = 1 + \frac{2}{\pi} \int_0^\infty exp\left(-\kappa u^2 t\right) \left[\frac{J_0(ur)Y_0(ua) - Y_0(ur)J_0(ua)}{J_0^2(ua) + Y_0^2(ua)}\right] \frac{du}{u}$$

In this context, $\kappa = k_r / \mu\phi\beta$, where k_r represents the rock permeability, μ is the fluid viscosity, ϕ is the porosity of the rock, and β is the fluid compressibility. Additionally, J_0 and Y_0 are the zero-order Bessel functions of the first and second kind, respectively.

For both infinite and zero pressurization rates, Ito's model provides the upper and lower bounds for breakdown pressure, as shown in Equations (7) and (8) [8].

$$P_b = \left(1 + \frac{d_c}{r_w}\right)^2 \left(\sigma_t - \sigma_\theta^1 - P_0\right) + P_0 \tag{7}$$

$$P_b = \frac{\sigma_t - \sigma_\theta^1 - P_0}{\frac{1}{2}\left\{1 + \left(1 + \frac{d_c}{r_w}\right)^2\right\}\left(2 - \frac{\alpha(1-2\nu)}{1-\nu}\right)} + P_0 \tag{8}$$

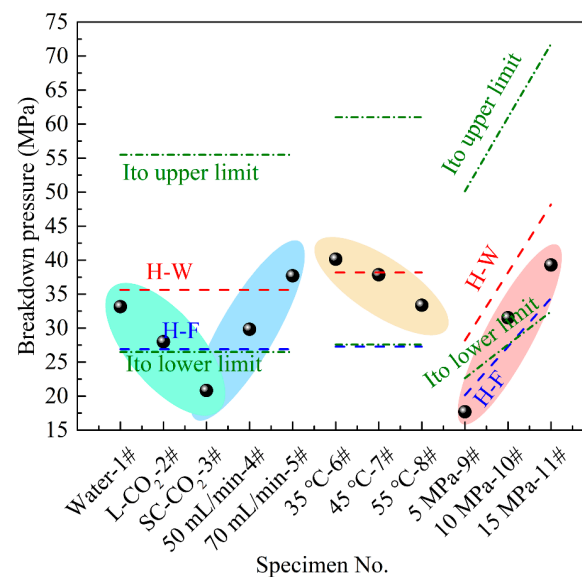### 3.2. Comparison of Theoretical and Experimental Results

As confirmed in the literature, the H-W, H-F, and Ito models yield reasonable estimates for calculating breakdown pressure. However, the fundamental assumptions underlying these models often fail to fully reflect real conditions. Moreover, breakdown pressure models based solely on tensile strength face challenges in accurately predicting the complex fracture processes involved. Consequently, a notable discrepancy exists between theoretical

predictions and experimental values [27,28]. To calculate the breakdown pressure corresponding to the theoretical models discussed, we combined experimental measurements with previously published results [35,36]. The parameters used for these calculations are detailed in Table 2, where the initial pore pressure was assumed to be 0 MPa.

Table 2. Parameters used in the theoretical models.

Parameters	Biot Coefficient	σ_t (MPa)	ν	r_w (m)	d_c (m)
Value	0.9	15.63 (1#~5#) 18.18 (6#~11#)	0.20 (1#~5#) 0.25 (6#~11#)	0.01	0.0024 (1#~5#) 0.0017 (6#~11#)

Figure 6 compares the breakdown pressure values obtained from laboratory experiments with those calculated using the aforementioned theoretical models. In Figure 6, the H-W model and H-F model are denoted as H-W and H-F, respectively. The H-W model assumes that the rock is either impermeable or possesses low permeability, while the H-F model assumes high permeability in the rock. It is evident from Figure 6 that the experimental data do not consistently fall within the theoretical ranges predicted by these models, indicating that classical breakdown pressure models fail to capture the anomalous phenomena observed during experiments. Several factors contribute to this discrepancy, as follows: (1) the assumptions underlying the theoretical models do not encompass all the influencing factors present in the experiments, and (2) these models, typically applied to hydraulic fracturing, may not be suitable for predicting breakdown pressure in SC-CO_2 fracturing.

Figure 6. Comparison between theoretical and experimental results. The areas shaded in green, blue, yellow, and red represent the scheme of fracturing fluid type, flow rate, temperature, and confining pressure, respectively. Black circle means the value of the breakdown pressure.

Various fracturing parameters such as the type of fracturing fluid, flow rate, temperature, and confining pressure significantly influence the experimental breakdown pressure values. For instance, an increase in the flow rate corresponds to a rise in breakdown pressure, as it relates to the rate of pressurization. Although the Ito model accounts for both pressurization rate and wellbore diameter, the upper and lower bounds of this model do not encompass the breakdown pressure for specimens 3 and 9 (Figure 6). This limitation may be attributed to the inherent heterogeneity of natural rock.

4. Breakdown Pressure Prediction with a Multi-Layer Neural Network

*4.1. Dataset Preparation and Model Verification*

As supported by Sampath et al. [28], theoretical models for calculating breakdown pressure are developed within different theoretical frameworks and assumptions, each focusing on a unique set of controlling factors. This variability restricts the applicability of these models. For example, the H-W model considers only horizontal principal stress, tensile strength, and pore pressure, while omitting factors such as wellbore diameter and pressurization rate. Although the Ito model incorporates wellbore diameter, it still assumes a constant pressurization rate and overlooks the impact of fracturing fluid temperature. As a result, numerous researchers have compared experimental data with breakdown pressures derived from these theoretical models, highlighting their inability to adequately account for abnormally high or low breakdown pressures observed during hydraulic and SC-CO_2 fracturing [37,38].

In other words, the fracturing of rock specimens during hydraulic fracturing and SC-CO_2 fracturing is a complex process involving the interaction of multiple factors. Currently, no comprehensive mathematical model encompasses all these variables for predicting breakdown pressure. Furthermore, established models indicate that not all influencing factors exhibit a linear relationship with breakdown pressure.

Similarly, the factors affecting fracturing effectiveness are numerous and interconnected in complex, nonlinear ways [39]. If breakdown pressure, a key indicator for fracturing effectiveness, could be predicted prior to experimentation or field operations, it would provide valuable reference data for optimizing fracturing design parameters. Presently, large-scale field fracturing experiments are costly and cannot be conducted repeatedly. Consequently, the trend leans towards small-scale laboratory experiments, which also require complex testing procedures and rock preparation [19]. Therefore, we aim to predict breakdown pressure under the influence of multiple factors by identifying the primary factors influencing breakdown pressure, collecting a substantial dataset from fracturing experiments, and employing neural networks to model the intricate nonlinear relationships between input and output variables.

Building upon extensive literature research [40–49] and our experimental data, we compiled a dataset consisting of 362 specimens. While this dataset provides a foundation for the model, it is insufficient for training a deep learning model. Therefore, special measures were taken to mitigate overfitting and improve model generalization, such as cross-validation, regularization, and parameter tuning [50].

The theoretical models discussed above do not account for vertical principal stress, the effect of wellbore diameter, and the minimal impact of the rock's elastic modulus on fracturing outcomes [14]. To address these limitations, we selected eight influencing factors for modeling: fracturing fluid type, maximum and minimum horizontal principal stresses, initial fracturing fluid temperature, wellbore diameter, flow rate, tensile strength, and Poisson's ratio of the specimens. Given the highly complex and nonlinear relationships between these factors and breakdown pressure, a simple multiple–linear regression approach would be insufficient. Therefore, we employed a multi-layer fully connected neural network, as illustrated in Figure 7, to learn representations from the experimental data. This neural network comprises three main components: an input layer (shown in orange), multiple hidden layers (shown in yellow and blue), and an output layer (shown in dark blue). The input layer receives data corresponding to the aforementioned eight influencing factors, which are then passed to the hidden layers through weighted connections (depicted by black arrows in Figure 7). In the hidden layers, each input is weighted, combined with a bias, and processed through an activation function to capture complex nonlinear relationships (illustrated by the diagram in the red frame in Figure 7). Finally, the output layer uses these transformed values to generate the predicted values for breakdown pressure.
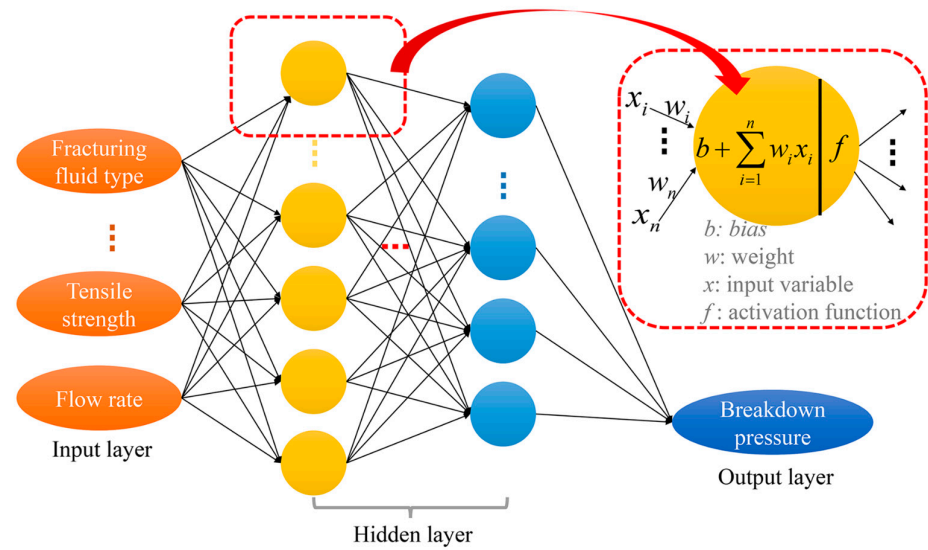
Figure 7. Schematic diagram of a multi-layer neural network model.

The model was implemented using the PyTorch deep learning framework (https://pytorch.org/) and coded in Python. To capture the nonlinear interactions among the variables, the ReLU activation function was introduced for two primary reasons, as follows: (1) if each layer's output were a linear function of its input, adding more hidden layers would not effectively represent the coupling effects of multiple factors on breakdown pressure, and (2) compared to traditional neural network activation functions such as the sigmoid function, ReLU promotes sparsity in the network, reducing overfitting and significantly improving training efficiency.

For preprocessing the raw data, two key aspects were considered:

- Normalization of input parameters—Since the influencing factors have varying dimensions and value ranges, normalization was necessary to prevent large fluctuations in model loss during backpropagation. The data were standardized based on the mean (μ) and standard deviation (σ) of the raw data (x) [51], as shown in the equation $x' = (x - \mu)/\sigma$, where x' represents the normalized data. This standardization process improves the model's convergence speed and accuracy. Notably, the fracturing fluid type was assigned numeric codes in descending order of viscosity;

- Splitting the dataset into training and testing sets—The training set was employed for model construction, parameter optimization, and variable updates, while the testing set was reserved for evaluating the model's performance and generalization ability, allowing for the detection of overfitting or underfitting. Data from the testing set were solely used for evaluation and did not affect model parameters. For this study, the dataset was split in a 7:3 ratio, with 250 samples allocated for training and 112 samples for testing. To fully utilize the entire dataset of 362 samples and validate the model with experimental results, the data obtained from 11 experimental groups were fixed as part of the testing set. An additional 101 samples were randomly selected from the remaining data to complete the testing set, resulting in a total of 112 testing samples, while the remaining 250 samples constituted the training set. Cross-validation was performed by using different random seeds to generate varying train–test splits. This process ensured the consistent generalization ability of the model, and aimed to achieve high accuracy and repeatability for subsequent test set analyses.

The loss function in deep learning [52] plays a critical role in assessing model convergence, training adequacy and the proper initialization of weights. In this study, the mean square error (*MSE*) function was adopted as the loss function, $MSE = \frac{1}{n}\sum_{i=1}^{n}\left(y_i - y_i^*\right)^2$, where n is the number of data points, y_i^* is the actual value, and y_i is the predicted value. The accuracy curve assesses the linear correlation between predicted and actual values

using the Pearson correlation coefficient [53]. By analyzing the trends in loss and accuracy across both the training and testing sets, we were able to determine whether the model underfits or overfits.

The maximum number of epochs for model training was set at 20,000, utilizing stochastic gradient descent as the optimizer with a learning rate of 0.0001. After conducting multiple tests with varying sample sizes and comparing the expected results, we selected a model consisting of three fully connected hidden layers, with 16, 16, and 12 neurons, respectively. The loss and accuracy results for the training and testing sets are shown in Figures 8 and 9. As illustrated, the loss function was initially high, but upon increasing the number of iterations, the error between the actual and predicted values decreased for both the training and testing sets, eventually stabilizing. After stabilization, both training and testing accuracy exceeded 90%, indicating that the multi-layer neural network model effectively learned and predicted breakdown pressure.

(a)

(b)
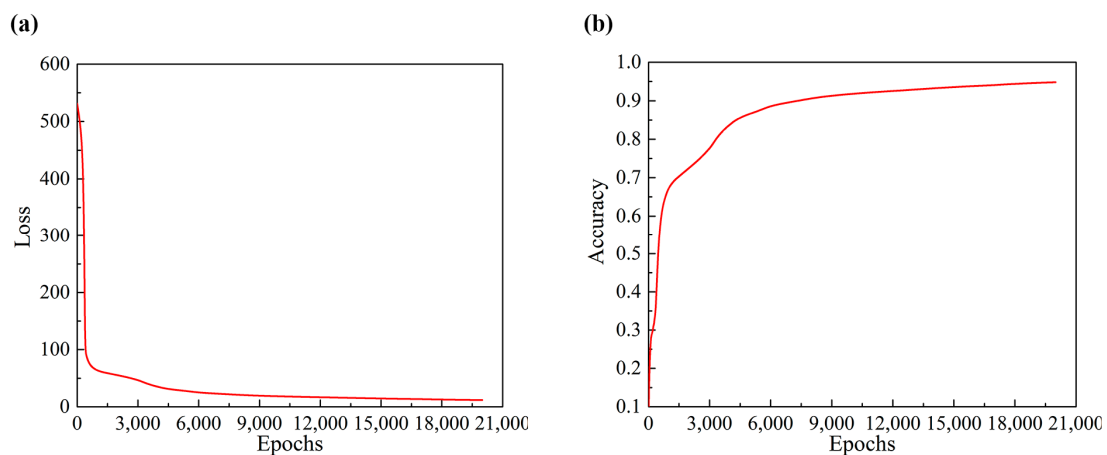
Figure 8. Performance of the neural network model on the training set: (**a**) Training loss curve, illustrating the model's reduction in prediction error across epochs, which demonstrates the model's learning process and its convergence toward minimizing error on known data; (**b**) training accuracy curve, showing the model's predictive accuracy on the training set over epochs, indicating the model's capacity to accurately capture the relationships between variables affecting breakdown pressure.

(a)

(b)
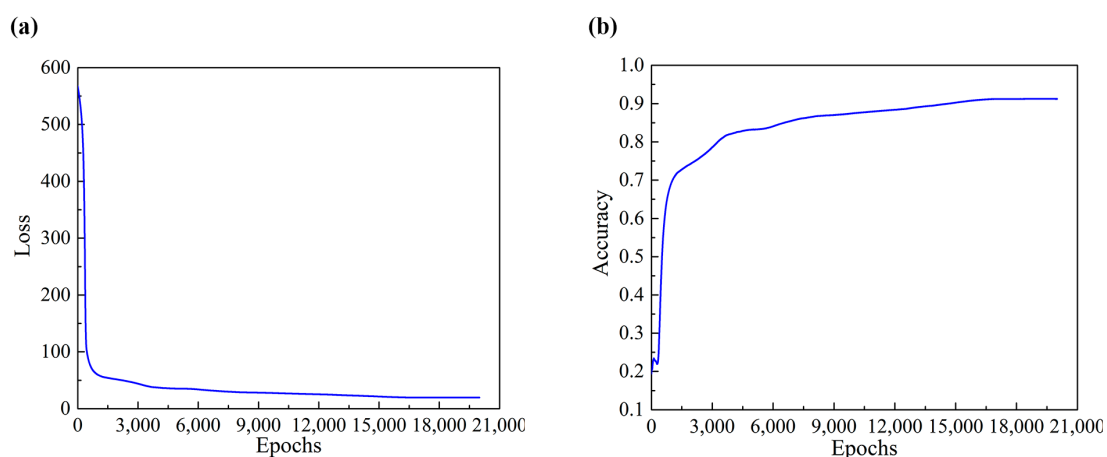
Figure 9. Performance of the neural network model on the testing set: (**a**) Testing loss curve, showing the reduction in prediction error across epochs, which indicates the model' ability to generalize and converge toward minimizing prediction error on unseen data; (**b**) testing accuracy curve, representing the model's predictive accuracy on the testing set over epochs, reflecting its capability to generalize and correctly predict breakdown pressure under various experimental conditions.

Metrics commonly used to evaluate prediction performance include the coefficient of determination (R), root mean square error ($RMSE$), and mean absolute error (MAE). A higher R value, closer to 1, indicates a stronger correlation between predicted and actual values, while lower $RMSE$ and MAE values reflect higher prediction accuracy. The formulae for these evaluation metrics are provided in Table 3, where n represents the number of data points, y_i^* and y_i are the actual and predicted values, respectively, and $\overline{y^*}$ and $\overline{y}$ represent the mean of actual and predicted values, respectively.

Table 3. Equations for calculating R, $RMSE$, and MAE.

| Index	Calculation
R	$R = \dfrac{\sum_{i=1}^{n}\left(y_i^*-\overline{y^*}\right)\left(y_i-\overline{y}\right)}{\sqrt{\sum_{i=1}^{n}\left(y_i^*-\overline{y^*}\right)^2}\sqrt{\sum_{i=1}^{n}\left(y_i-\overline{y}\right)^2}}$
$RMSE$	$RMSE = \sqrt{\dfrac{1}{n}\sum_{i=1}^{n}\left(y_i-y_i^*\right)^2}$
MAE	$MAE = \dfrac{1}{n}\sum_{i=1}^{n}\left|y_i^*-y_i\right|$

To further validate the prediction performance of the trained model, we compared the predicted values from the training set with the actual values and performed a regression analysis of the predicted versus actual values for the testing set. The coefficients R, $RMSE$, and MAE were calculated, as shown in Table 3. Figure 10 illustrates that the data points for both the training and testing samples are closely aligned with the ideal fit line, where the actual value equals the predicted value. The R, $RMSE$, and MAE values for the training set (testing set) were 0.9482 (0.9123), 3.424 (4.421), and 2.283 (3.188), respectively.
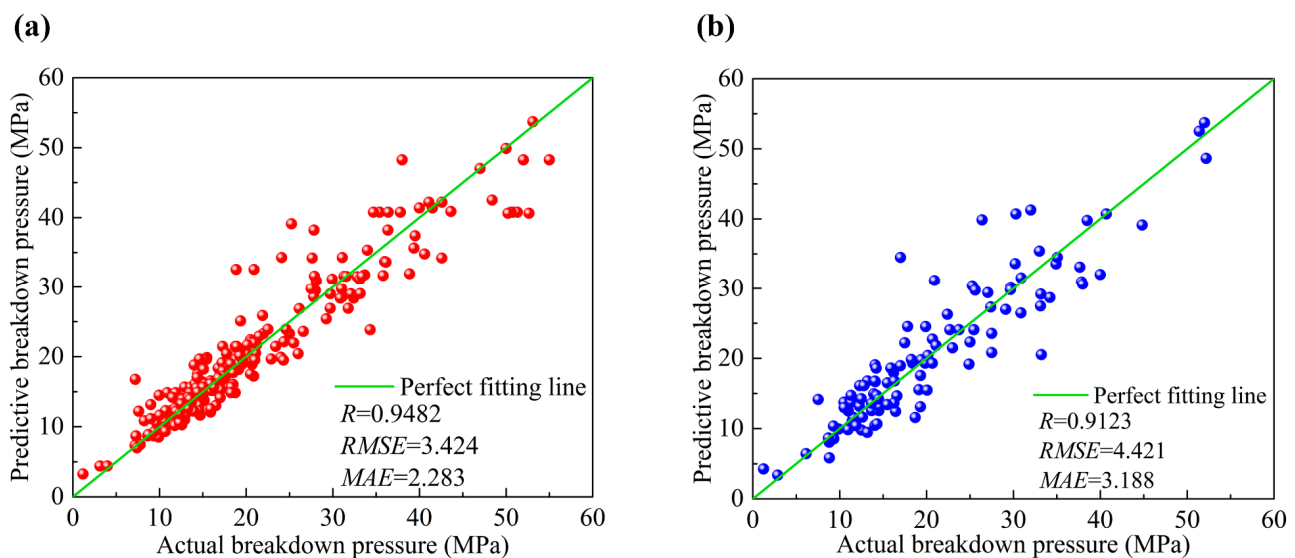
Figure 10. Correlation between actual values and predictive values: (**a**) Training dataset; (**b**) predicting dataset.

Compared to the PSO-BPNN model in the literature [19], which achieved an R value of 0.6971 for the test set, the multi-layer neural network improved the R value by 23.6%. These results demonstrate the neural network's effectiveness in learning and predicting breakdown pressure, indicating the strong predictive capability of the trained model.

Notably, Figure 11 shows the model's predicted breakdown pressure for the fracturing experiments, with an average relative error of approximately 16% between the predicted and experimental values. This highlights the model's accuracy in predicting breakdown pressure and its potential as an effective tool for optimizing fracturing operation parameters.
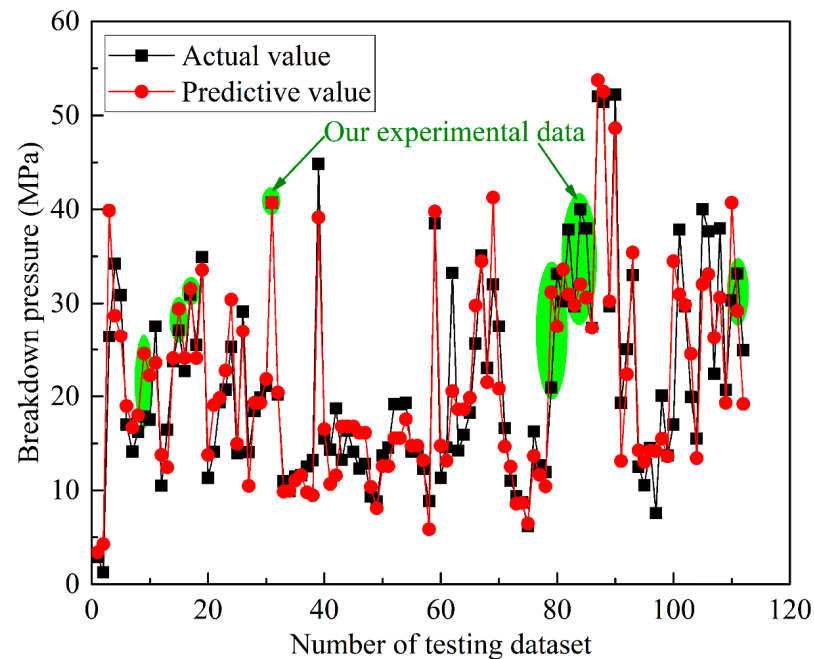
Figure 11. Comparison of actual values and predictive values.

4.2. Relative Importance of Influencing Variables

Following the method proposed by Yan et al. [54], the procedure for quantifying the relative importance of the eight influencing factors mentioned earlier involves the following steps:

Step 1—Keep all other variables constant while increasing or decreasing the input variable under analysis by 10% from its original value in the training dataset, generating two new input datasets;

Step 2—Apply the trained neural network model to compute the results for these two datasets and calculate the difference between them. The greater the difference, the more significant the influence of that variable on the output;

Step 3—Repeat this process for each input variable, then compute the average difference across all variables. The mean difference provides a measure of each input variable's influence on the predicted outcome.

As illustrated in Figure 12, the relative importance of the factors is ranked as follows: fracturing fluid type > tensile strength > flow rate > maximum horizontal stress > Poisson's ratio > wellbore diameter > minimum horizontal stress > initial fracturing fluid temperature. Specifically, fracturing fluid type and tensile strength are the most sensitive variables, contributing 28.31% and 21.39% of the influence, respectively. This is due to the significant role of fracturing fluid properties in establishing the pore pressure system within the rock, and the critical impact of effective stress on fracture initiation. Tensile strength directly determines the rock's failure resistance, as it defines the relationship between effective circumferential stress at the wellbore or characteristic distance and the rock's ability to resist failure [28].

The flow rate accounted for 12.34% of the influence on breakdown pressure, as different fracturing fluids exhibit varying compressibility, resulting in distinct effects on pressure buildup within the same injection time. The initial fracturing fluid temperature had a minimal impact, likely due to two reasons: (1) the dataset included multiple types of fracturing fluids, with temperature variation closely tied to the fluid type, and (2) for SC-CO_2, the initial temperature only reflects pre-injection conditions, without accounting for temperature changes during the fracturing process, which significantly affect fracturing performance.
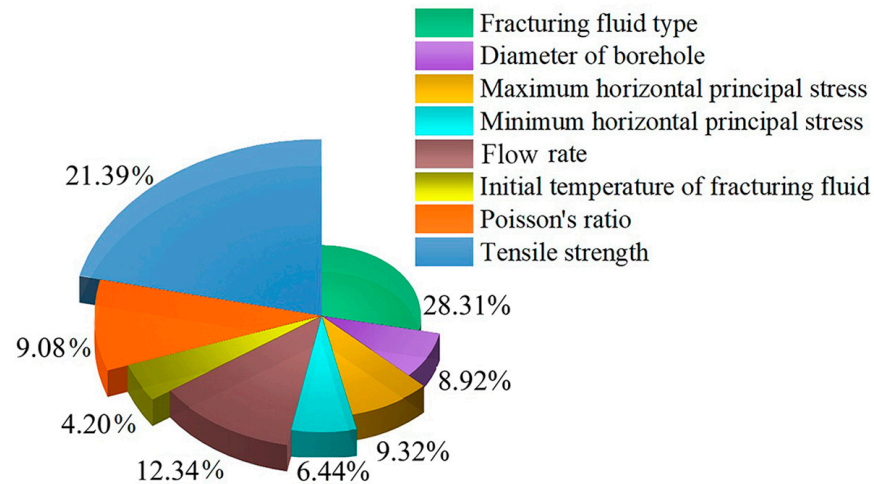
Figure 12. The relative importance of influencing variables.

Although the multi-layer neural network model built in this study achieved high predictive accuracy, the experimental data used were limited. Moreover, many key parameters (e.g., fracture toughness, permeability) that are crucial in the fracturing process were not included in the available literature. Future studies should expand the dataset and comprehensively test the mechanical properties of rocks used in fracturing experiments. Predicting the effects of multiple factors on breakdown pressure using deep learning represents a notable advancement in understanding the complex relationships between variables in fracturing operations.

By quantifying the relative importance of factors such as fluid type, tensile strength, and flow rate, the trained neural network model provides valuable insights into their interactions. This knowledge can guide the optimization of fracturing parameters for more efficient and effective operations. The findings of this study align with those from previous research, which indicates that key variables like fluid type and rock strength disproportionately affect breakdown pressure. This can be attributed to the distinct properties and interactions of SC-CO$_2$ with rock formations. SC-CO$_2$, with its low viscosity and high diffusivity, penetrates microfractures and rock fissures more efficiently than water-based fluids, thereby lowering the breakdown pressure required for fracture initiation. This property is especially beneficial for rocks with high tensile strength, where conventional fluids are less effective in initiating fractures due to limited penetrative ability. Additionally, tensile strength significantly influences the pressure threshold for fracture initiation. Higher tensile strength requires increased breakdown pressure, which SC-CO$_2$ mitigates through its superior infiltration capability and stress-reducing properties. These characteristics enable SC-CO$_2$ to overcome the resistance posed by high tensile strength, enhancing fracturing performance in formations that are challenging for use in traditional hydraulic fracturing. By incorporating various fluid types, flow rates, and stress conditions, this study provides a more nuanced understanding of how different factors contribute to fracturing outcomes. Moreover, the use of data-driven, deep learning techniques offers a flexible and adaptable approach to predicting breakdown pressure, particularly in the context of SC-CO$_2$ fracturing, where traditional models often fall short. The trained neural network model serves as a decision-support tool, enabling engineers to simulate fracturing outcomes under various parameter settings before field implementation. This application minimizes trial-and-error in parameter selection and improves operational efficiency by predicting optimal conditions for SC-CO$_2$ fracturing, such as ideal injection rates and pressure levels. By accurately predicting breakdown pressure, the model ensures safe, cost-effective fracturing operations while maximizing resource extraction.

5. Conclusions

This study presents an integrated approach to predicting breakdown pressure in SC-CO_2 fracturing by combining experimental data with a multi-layer neural network model. The findings confirm that SC-CO_2 exhibits superior fracturing performance compared to traditional hydraulic fracturing fluids, primarily due to its high diffusivity and effective infiltration of microfractures, thereby lowering the breakdown pressure required for fracture initiation. Elevated confining pressures significantly increase breakdown pressure, highlighting the critical role of in situ stress. Additionally, the study found that higher flow rates also led to higher breakdown pressures, suggesting that increased flow rates enable the faster build-up of injection pressure, thus causing rock failure more rapidly. The effect of temperature was also evident, with breakdown pressure decreasing as temperature increased, indicating that higher temperatures facilitate fracturing by reducing the effective stress in the rock.

A comparison of experimental results with theoretical predictions from the H-W and H-F models revealed discrepancies, indicating that classical breakdown pressure models fail to fully capture the complex phenomena observed during SC-CO_2 fracturing. This is partly because these models were originally designed for hydraulic fracturing and operate under simplifying assumptions, such as low or high rock permeability, which may not align with actual experimental conditions. Moreover, the Ito model, which incorporates parameters, such as pressurization rate and wellbore diameter, also failed to predict the breakdown pressures of certain specimens, likely due to the inherent heterogeneity of natural rock.

Using a fully connected neural network, this study successfully captured the nonlinear relationships among multiple influencing factors (fracturing fluid type, flow rate, temperature, tensile strength, and confining pressure) and the breakdown pressure. The model outperformed traditional predictive models, achieving an *R* value of 0.9123 for the testing set, thereby demonstrating strong predictive capability. The sensitivity analysis identified fracturing fluid type and tensile strength as the most influential factors, contributing 28.31% and 21.39% to the overall breakdown pressure, respectively. These insights offer a data-driven foundation for optimizing fracturing design and improving operational efficiency.

Despite promising results, this study acknowledges limitations, including the relatively small dataset size and the exclusion of critical parameters such as fracture toughness and rock permeability. Future research should expand the dataset and incorporate a more comprehensive range of rock properties to further enhance the model's predictive accuracy. Overall, the application of a multi-layer neural network model provides a robust, adaptable framework for predicting fracturing outcomes, particularly for unconventional fracturing techniques such as SC-CO_2, as traditional models often fail to account for complex variable interactions.

Author Contributions: Conceptualization, X.Z.; methodology, X.Z.; software, M.Z.; validation, S.L. and H.L.; formal analysis, X.Z. and M.Z.; investigation, H.L.; resources, X.Z.; data curation, M.Z.; writing—original draft preparation, X.Z.; writing—review and editing, M.Z. and S.L.; visualization, X.Z. and M.Z.; supervision, S.L.; project administration, X.Z.; funding acquisition, X.Z. All authors have read and agreed to the published version of the manuscript.

**Institutional Review Board Statement:** Not applicable.

Informed Consent Statement: Not applicable.

Data Availability Statement: The original contributions presented in the study are included in the article, further inquiries can be directed to the corresponding author.

Conflicts of Interest: The authors declare no conflicts of interest.

Appendix A

As illustrated in Figure A1, the total circumferential stress around the borehole consists of three components, as follows: (1) the circumferential stress component (σ_θ^1) resulting from the maximum and minimum horizontal stresses (σ_H and σ_h); (2) the circumferential stress component (σ_θ^2) generated by the injection pressure of the fracturing fluid (P_w); and (3) the circumferential stress component (σ_θ^3) induced by the pore pressure distribution (p) within the rock. The stress distribution in σ_θ^1 can be visualized as acting on the edges of a large rectangular plate containing a central circular hole. In σ_θ^2, the wellbore pressure rises from the original pore pressure (P_0) to the injection pressure (P_w). Finally, σ_θ^3 represents the radial fluid flow into the rock when there is a pressure differential between the injected fluid and the pore fluid, leading to an additional stress component.
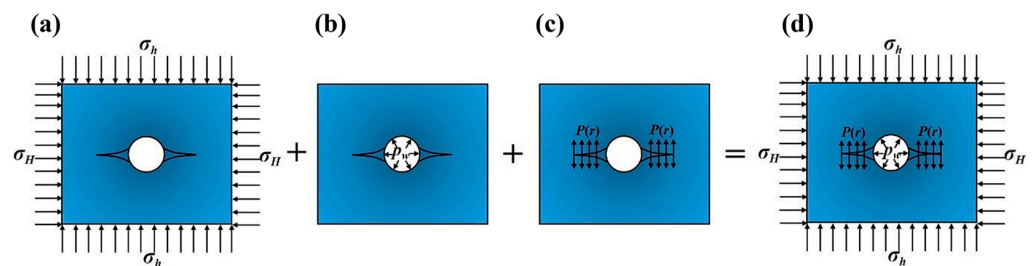
Figure A1. Stress distribution leading to rock formation breakdown: (**a**) In situ circumferential stress field resulting from the maximum and minimum horizontal stresses; (**b**) circumferential stress induced by the injection pressure of the fracturing fluid within the wellbore; (**c**) circumferential stress attributed to pore pressure distribution throughout the rock mass; (**d**) total circumferential stress distribution after the superimposition of all three components [28].

The in situ circumferential total stress field (σ_θ^1), resulting from the maximum and minimum horizontal stresses, is calculated using Equation (A1) [28],

$$\sigma_\theta^1 = \left(\frac{\sigma_H + \sigma_h}{2}\right)\left(1 + \frac{r_w^2}{r^2}\right) - \left(\frac{\sigma_H - \sigma_h}{2}\right)\left(1 + \frac{3r_w^4}{r^4}\right)cos2\theta + P_0 \tag{A1}$$

where σ_H and σ_h represent the maximum and minimum horizontal stresses, respectively, with the condition $|\sigma_H| > |\sigma_h|$. The angle θ is measured counterclockwise from the direction of σ_H, where $\theta = 0$ corresponds to the σ_H direction. The variable r_w denotes the borehole radius, while r represents the horizontal radial distance from the center of the hole.

The circumferential total stress (σ_θ^2) induced by the injection pressure of the fracturing fluid in the wellbore is calculated using Equation (A2),

$$\sigma_\theta^2 = \frac{r_w^2 r_e^2 p_w}{r^2(r_e^2 - r_w^2)} - \frac{r_w^2 p_w}{r_e^2 - r_w^2} \tag{A2}$$

where r_e is the radius of the far-field boundary, and p_w is the pressure difference between the injected fluid pressure and the reservoir pore pressure, defined as $p_w = P_w - P_0$.

The circumferential total stress (σ_θ^3), arising from the pore pressure distribution within the rock mass, is calculated using Equation (A3),

$$\sigma_\theta^3 = \frac{\alpha(1 - 2\nu)}{r^2(1 - \nu)}\left[\left(\frac{r^2 + r_w^2}{r_e^2 - r_w^2}\right)\int_{r_w}^{r_e} p(r)rdr + \int_{r_w}^{r} p(r)rdr - p(r)r^2\right] \tag{A3}$$

where ν is the Poisson's ratio of the reservoir, α is the Biot coefficient, ranging from 0 to 1, and $p(r)$ is the pore pressure at a radial distance r from the center of the wellbore, exceeding the original pore pressure P_0, such that $p(r) = P_r - P_0$.

The circumferential effective stress (σ_θ) is the sum of these three stress components minus the original pore pressure P_0, as shown in Equation (A4).

$$\sigma_\theta = \sigma_\theta^1 + \sigma_\theta^2 + \sigma_\theta^3 - P_0 \tag{A4}$$

Assuming that the far-field boundary r_e is significantly larger than the wellbore radius r_w, the circumferential stress components σ_θ^2 and σ_θ^3 can be expressed in simplified forms as follows:

$$\sigma_\theta^2 = -\frac{r_w^2 p_w}{r^2} \tag{A5}$$

$$\sigma_\theta^3 = \frac{\alpha(1-2\nu)}{r^2(1-\nu)}\left[\int_{r_w}^{r} p(r)r\,dr - p(r)r^2\right] \tag{A6}$$

References

1. Middleton, R.S.; Carey, J.W.; Currier, R.P.; Hyman, J.D.; Kang, Q.; Karra, S.; Jiménez-Martínez, J.; Porter, M.L.; Viswanathan, H.S. Shale gas and non-aqueous fracturing fluids: Opportunities and challenges for supercritical CO_2. *Appl. Energy* **2015**, *147*, 500–509. [CrossRef]
2. Wang, H.; Li, G.; Shen, Z. A feasibility analysis on shale gas exploitation with supercritical carbon dioxide. *Energy Sources Part A Recover. Util. Environ. Eff.* **2012**, *34*, 1426–1435. [CrossRef]
3. Sun, B.; Wang, J.; Sun, W.; Wang, Z.; Sun, J. Advances in fundamental research of supercritical CO_2 fracturing technology for unconventional natural gas reservoirs. *J. China Univ. Pet.* **2019**, *43*, 82–91. [CrossRef]
4. Li, S.; Zhang, D. How effective is carbon dioxide as an alternative fracturing fluid? *SPE J.* **2018**, *24*, 857–876. [CrossRef]
5. Zhou, D. The Influence of Supercritical CO_2 Phase Change on Growth of Multiscale Fractures. Ph.D. Thesis, China University of Petroleum, Beijing, China, 2020.
6. Hubbert, M.K.; Willis, D.G. Mechanics of hydraulic fracturing. *Trans. AIME* **1957**, *210*, 153–168. [CrossRef]
7. Haimson, B.; Fairhurst, C. Initiation and extension of hydraulic fractures in rocks. *Soc. Pet. Eng. J.* **1967**, *7*, 310–318. [CrossRef]
8. Ito, T. Effect of pore pressure gradient on fracture initiation in fluid saturated porous media: Rock. *Eng. Fract. Mech.* **2008**, *75*, 1753–1762. [CrossRef]
9. Li, X.; Feng, Z.; Han, G.; Elsworth, D.; Marone, C.; Saffer, D.; Cheon, D.-S. Breakdown pressure and fracture surface morphology of hydraulic fracturing in shale with H_2O, CO_2 and N_2. *Geomech. Geophys. Geo-Energy Geo-Resour.* **2016**, *2*, 63–76. [CrossRef]
10. Chen, L.; Tian, S.; Li, G.; Fan, X. Initiation pressure models for supercritical CO_2 fracturing and sensitivity analysis. *Rock Soil Mech.* **2015**, *36*, 125–131. [CrossRef]
11. Zhang, S.; Chen, Z. Application status and prospect of artificial intelligence in reservoir stimulation. *Pet. Drill. Tech.* **2023**, *51*, 69–77. [CrossRef]
12. Li, Q.; Zhu, Z. Calibration of an elastoplastic model of sand liquefaction using the swarm intelligence with a multi-objective function. *J. Rock Mech. Geotech. Eng.* **2023**, *15*, 789–802. [CrossRef]
13. Guo, D.; Tang, Y.; Li, S.; Zhang, T.; Kang, Y. Optimization of tight gas fracturing operation parameters based on BP-PSO. *Sci. Technol. Eng.* **2022**, *22*, 8304–8312. Available online: https://apps.wanfangdata.com.cn/perios/article:kxjsygc202219019 (accessed on 10 November 2024).
14. Yan, H.; Zhang, J.; Zhou, N.; Shi, P. SC-CO_2 fracturing effect prediction of coal and rock mass based on DA-DE-SVM intelligent model. *Chin. J. Geotech. Eng.* **2022**, *45*, 362–368. [CrossRef]
15. Hui, G.; Chen, S.; Wang, H.; Gu, F. Application of improved residual neural network-based machine learning method in the prediction of shale gas sweet spot. *J. Southwest Pet. Univ.* **2021**, *43*, 19–32. Available online: https://www.sciengine.com/JSUST/doi/10.11885/j.issn.1674-5086.2021.02.27.01 (accessed on 10 November 2024).
16. Jiang, T.; Zhou, J.; Liao, L. Development status and future trends of intelligent fracturing technologies. *Pet. Drill. Tech.* **2022**, *50*, 1–9. [CrossRef]
17. Gao, A. Research on the Prediction Model of the Fracturing Effect Based on Extra High Water cut Stage in South Eight area. Master's Thesis, Northeast Petroleum University, Daqing, China, 2013.
18. Yan, H. Staged Cracking Mechanism and Crack Propagation Law of Supercritical CO_2 Fracturing Coal Mass. Ph.D. Thesis, China University of Mining and Technology, Xuzhou, China, 2020.
19. Yan, H.; Zhang, J.; Zhou, N.; Li, B.; Wang, Y. Crack initiation pressure prediction for SC-CO_2 fracturing by integrated meta-heuristics and machine learning algorithms. *Eng. Fract. Mech.* **2021**, *249*, 107750. [CrossRef]
20. LeCun, Y.; Bengio, Y.; Hinton, G. Deep learning. *Nature* **2015**, *521*, 436–444. [CrossRef]
21. Zhu, W.; Zhang, X.; Liu, S.; Wei, C.; Wang, J.; Liu, H. An experimental apparatus for supercritical CO_2 fracturing of shale: System design and application tests. *J. Nat. Gas Sci. Eng.* **2022**, *103*, 104656. [CrossRef]
22. Zhang, X.; Zhu, W.; Xu, Z.; Liu, S.; Wei, C. A review of experimental apparatus for supercritical CO_2 fracturing of shale. *J. Pet. Sci. Eng.* **2022**, *208*, 109515. [CrossRef]

23. Hu, Y. Mechanism and Experimental Research of Supercritical Carbon Dioxide Fracturing Shale. Ph.D. Thesis, Wuhan University, Wuhan, China, 2017.

24. Detournay, E.; Carbonell, R. Fracture-mechanics analysis of the breakdown process in minifracture or leakoff test. *SPE Prod. Facil.* **1997**, *12*, 195–199. [CrossRef]

25. Chen, Z.; Elsworth, D.; Wang, M. Does low-viscosity fracturing fluid always create complex fractures? *J. Geophys. Res. Solid Earth* **2020**, *125*, e2020JB020332. [CrossRef]

26. Lu, Y.; Liao, Y.; Tang, J.; Zhang, X.; Han, S.; Ling, Y. Experimental study on fracture initiation pressure and morphology in shale using supercritical CO_2 fracturing. *J. China Coal Soc.* **2018**, *43*, 175–180. [CrossRef]

27. Wu, F.; Meng, P.; Ding, Q.; Li, D.; Yang, W. Calculating models of the breakdown pressure for hydraulic fracturing. *Pet. Geol. Oilfield Dev. Daqing* **2020**, *39*, 59–68. [CrossRef]

28. Sampath, K.H.S.M.; Perera, M.S.A.; Ranjith, P.G. Theoretical overview of hydraulic fracturing break-down pressure. *J. Nat. Gas Sci. Eng.* **2018**, *58*, 251–265. [CrossRef]

29. Guo, Z.; Tian, S.; Liu, Q.; Ma, L.; Yong, Y.; Yang, R. Experimental investigation on the breakdown pressure and fracture propagation of radial borehole fracturing. *J. Pet. Sci. Eng.* **2022**, *208*, 109169. [CrossRef]

30. Zhuang, L.; Kim, K.Y.; Shin, H.S.; Jung, S.G.; Diaz, M. Experimental investigation of effects of borehole size and pressurization rate on hydraulic fracturing breakdown pressure of granite. In Proceedings of the 10th Asian Rock Mechanics Symposium, Singapore, 29 October–3 November 2018.

31. Haimson, B.C.; Zhao, Z. Effect of borehole size and pressurization rate on hydraulic fracturing breakdown pressure. In Proceedings of the 32nd U.S. Symposium on Rock Mechanics (USRMS), Norman, OK, USA, 10–12 July 1991; pp. 191–199.

32. Garagash, D.; Detournay, E. An analysis of the influence of the pressurization rate on the borehole breakdown pressure. *Int. J. Solids Struct.* **1997**, *34*, 3099–3118. [CrossRef]

33. Garagash, D.; Detournay, E. Influence of pressurization rate on borehole breakdown pressure in impermeable rocks. In Proceedings of the 2nd North American Rock Mechanics Symposium, Montreal, QC, Canada, 19–21 June 1996.

34. Jia, Y.; Song, C.; Wang, J.; Gan, Q. The breakdown process of low-permeable shale and high-permeable sandstone rocks due to non-aqueous fracturing: The role of fluid infiltration. *J. Nat. Gas Sci. Eng.* **2021**, *89*, 103873. [CrossRef]

35. Ranjith, P.G.; Zhang, C.P.; Zhang, Z.Y. Experimental study of fracturing behaviour in ultralow permeability formations: A comparison between CO_2 and water fracturing. *Eng. Fract. Mech.* **2019**, *217*, 106541. [CrossRef]

36. Wang, L.; Yao, B.; Xie, H.; Winterfeld, P.H.; Kneafsey, T.J.; Yin, X.; Wu, Y.-S. CO_2 injection-induced fracturing in naturally fractured shale rocks. *Energy* **2017**, *139*, 1094–1110. [CrossRef]

37. Wanniarachchi, W.; Gamage, R.; Perera, M.; Rathnaweera, T.; Gao, M.; Padmanabhan, E. Investigation of depth and injection pressure effects on breakdown pressure and fracture permeability of shale reservoirs: An experimental study. *Appl. Sci.* **2017**, *7*, 664. [CrossRef]

38. Morita, N.; Black, A.D.; Fuh, G.-F. Borehole breakdown pressure with drilling fluids—I. Empirical results. *Int. J. Rock Mech. Min. Sci. Geomech. Abstr.* **1996**, *33*, 39–51. [CrossRef]

39. Sun, D.; Wang, H.; Hou, M.; Zhao, W.; Song, Q.; Liu, Z.; Niu, S. Factors influence the effects of hydrofracturing in a low-permeability oilfield and potential evaluation using artificial neural network. *J. Geomech.* **2006**, *12*, 485–491.

40. Zhang, C.P.; Cheng, P.; Ma, Z.Y.; Ranjith, P.G.; Zhou, J.P. Comparison of fracturing unconventional gas reservoirs using CO_2 and water: An experimental study. *J. Pet. Sci. Eng.* **2021**, *203*, 108598. [CrossRef]

41. Jia, Y.; Lu, Y.; Elsworth, D.; Fang, Y.; Tang, J. Surface characteristics and permeability enhancement of shale fractures due to water and supercritical carbon dioxide fracturing. *J. Pet. Sci. Eng.* **2018**, *165*, 284–297. [CrossRef]

42. Zhang, Y.; He, J.; Li, X.; Lin, C. Experimental study on the supercritical CO_2 fracturing of shale considering anisotropic effects. *J. Pet. Sci. Eng.* **2019**, *173*, 932–940. [CrossRef]

43. Chong, Z.; Yao, Q.; Li, X. Experimental investigation of fracture propagation behavior induced by hydraulic fracturing in anisotropic shale cores. *Energies* **2019**, *12*, 976. [CrossRef]

44. Zhao, Z.; Li, X.; He, J.; Mao, T.; Zheng, B.; Li, G. A laboratory investigation of fracture propagation induced by supercritical carbon dioxide fracturing in continental shale with interbeds. *J. Pet. Sci. Eng.* **2018**, *166*, 739–746. [CrossRef]

45. Jiang, Y.; Qin, C.; Kang, Z.; Zhou, J.; Li, Y.; Liu, H.; Song, X. Experimental study of supercritical CO_2 fracturing on initiation pressure and fracture propagation in shale under different triaxial stress conditions. *J. Nat. Gas Sci. Eng.* **2018**, *55*, 382–394. [CrossRef]

46. Zhang, X.; Lu, Y.; Tang, J.; Zhou, Z.; Liao, Y. Experimental study on fracture initiation and propagation in shale using supercritical carbon dioxide fracturing. *Fuel* **2017**, *190*, 370–378. [CrossRef]

47. Wang, L.; Yao, B.; Xie, H.; Kneafsey, T.J.; Winterfeld, P.H.; Yin, X.; Wu, Y.-S. Experimental investigation of injection-induced fracturing during supercritical CO_2 sequestration. *Int. J. Greenh. Gas Control* **2017**, *63*, 107–117. [CrossRef]

48. Zhou, D.; Zhang, G.; Wang, Y.; Xing, Y. Experimental investigation on fracture propagation modes in supercritical carbon dioxide fracturing using acoustic emission monitoring. *Int. J. Rock Mech. Min. Sci.* **2018**, *110*, 111–119. [CrossRef]

49. Bing, Y.; Haizhu, W.; Zhonghou, S.; Qun, L.; Yong, Z.; Lujie, S. The supercritical CO_2 fracturing experimental study on fracture initiation of different rocks. In Proceedings of the 53rd US Rock Mechanics/Geomechanics Symposium, New York, NY, USA, 23–26 June 2019.

50. Halevy, A.; Norvig, P.; Pereira, F. The unreasonable effectiveness of data. *IEEE Intell. Syst.* **2009**, *24*, 8–12. [CrossRef]

51. Anysz, H.; Zbiciak, A.; Ibadov, N. The influence of input data standardization method on prediction accuracy of artificial neural networks. *Procedia Eng.* **2016**, *153*, 66–70. [CrossRef]

52. Son, S.; Jeong, Y.; Cho, S.K.; Lee, J.I. Development of supercritical CO_2 turbomachinery off-design model using 1D mean-line method and Deep Neural Network. *Appl. Energy* **2020**, *263*, 114645. [CrossRef]

53. Wang, Y.; Zhao, J.; Yang, C.; Xu, D.; Ge, J. Remaining useful life prediction of rolling bearings based on Pearson correlation-KPCA multi-feature fusion. *Measurement* **2022**, *201*, 111572. [CrossRef]

54. Yan, H.; Zhang, J.; Rahman, S.S.; Zhou, N.; Suo, Y. Predicting permeability changes with injecting CO_2 in coal seams during CO_2 geological sequestration: A comparative study among six SVM-based hybrid models. *Sci. Total Environ.* **2020**, *705*, 135941. [CrossRef]